

OVER-SIZED GAS CLUMPS IN AN EXTREMELY-METAL-POOR MOLECULAR CLOUD REVEALED BY ALMA'S PC-SCALE MAPS

YONG SHI,^{1,2} JUNZHI WANG,³ ZHI-YU ZHANG,^{1,2} QIZHOU ZHANG,⁴ YU GAO,^{5,6} LUWENJIA ZHOU,^{1,2} QIUSHENG GU,^{1,2}
KEPING QIU,^{1,2} XIAO-YANG XIA,⁷ CAI-NA HAO,⁷ AND YANMEI CHEN^{1,2}

¹*School of Astronomy and Space Science, Nanjing University, Nanjing 210093, China.*

²*Key Laboratory of Modern Astronomy and Astrophysics (Nanjing University), Ministry of Education, Nanjing 210093, China.*

³*Shanghai Astronomical Observatory, Chinese Academy of Sciences, 80 Nandan Road, Shanghai 200030, China*

⁴*Center for Astrophysics | Harvard & Smithsonian, 60 Garden Street, Cambridge MA 02138, USA*

⁵*Department of Astronomy, Xiamen University, Xiamen, Fujian 361005, China*

⁶*Purple Mountain Observatory, Chinese Academy of Sciences, Nanjing 210008, China*

⁷*Tianjin Astrophysics Center, Tianjin Normal University, Tianjin 300387*

Submitted to ApJ

ABSTRACT

Metals are thought to have profound effects on the internal structures of molecular clouds in which stars are born. The absence of metals is expected to prevent gas from efficient cooling and fragmentation in theory. However, this effect has not yet been observed at low metallicity environments, such as in the early Universe and local dwarf galaxies, because of the lack of high spatial resolution maps of gas. We carried out ALMA observations of the carbon monoxide (CO) $J=2-1$ emission line at 1.4-parsec resolutions of a molecular cloud in DDO 70 at 7% solar metallicity, the most metal-poor galaxy currently known with a CO detection. In total, five clumps have been identified and they are found to follow more or less the Larson's law. Since the CO emission exists in regions with visual extinction A_V around 1.0, we converted this A_V to the gas mass surface density using a gas-to-dust ratio of $4,594 \pm 2,848$ for DDO 70. We found that the CO clumps in DDO 70 exhibit significantly larger (on average four times) sizes than those at the same gas mass surface densities in massive star-formation regions of the Milky Way. The existence of such large clumps appears to be consistent with theoretical expectations that gas fragmentation in low metallicity clouds is suppressed. While our observation is only for one cloud in the galaxy, if it is representative, the above result implies suppressed gas fragmentation during the cloud collapse and star formation in the early Universe.

Keywords: galaxies: dwarf galaxies: ISM submillimeter: ISM

1. INTRODUCTION

Across the cosmic time, the rate of star formation first rises until redshift of ~ 2 and then drops toward the present time (Madau & Dickinson 2014). The majority of cosmic star formation takes place in galaxies with lower stellar masses and metallicity than our Milky Way (Sobral et al. 2014), especially for star formation in the early Universe (Knudsen et al. 2016; Inoue et al. 2016). Formation of stars is a local process, taking place within clouds of molecular gas with sizes of only tens of parsecs (pcs). Metals (elements heavier than helium) are expected to have profound effects on the internal structure of a molecular cloud and its collapse into stars (Omukai et al. 2005; Glover, & Clark 2012): metal poor gas is expected to be warmer due to inefficient cooling and the fragmentation is expected to be suppressed. However, studies of nearby galaxies have not seen such an effect because of a lack of high spatial-resolution gas maps of extremely metal-poor galaxies (Rubio et al. 2015; Schruba et al. 2017). Using the Atacama Large Millimeter/sub-millimeter Array (ALMA), we resolved a molecular cloud in an extremely metal-poor galaxy DDO 70 at a scale of 1.4 pc. This resolution is sufficient to resolve the Jeans fragmentation with a typical length of ~ 3.5 pc assuming $T=30$ K and $n(H_2)=10^2$ cm $^{-3}$ (Zhang et al. 2009).

DDO 70 is a nearby dwarf irregular galaxy at a distance of 1.38 Mpc (Tully et al. 2013). It has a total stellar mass of $10^{7.56} M_\odot$ (Cook et al. 2014) and a gas-phase oxygen abundance of 7% of the solar value (Kniazev et al. 2005). Previously we have targeted a star-forming region in this galaxy as shown in Figure 1 to search for the CO $J=2-1$ emission with the Institut de Radioastronomie Millimetrique (IRAM) 30-m telescope (Shi et al. 2016), whose detection provides direct evidence for the existence of molecular gas at such a low metallicity. It is currently the most metal-poor galaxy with a CO detection (Elmegreen et al. 2013; Rubio et al. 2015; Shi et al. 2015; Schruba et al. 2017). This single-dish detection offers an opportunity to resolve the molecular cloud with ALMA.

2. DATA

2.1. ALMA data of DDO 70

To probe the internal structure of the star-forming region in DDO 70, we resolved the CO $J=2-1$ emission using the ALMA with a field of view of $26.4''$ (177 pc) as shown in Figure 1. The ALMA observations (PID: 2016.1.00359.S, PI: Y. Shi) were composed of two array configurations of C40-4 and C40-7, which have an angular resolution of 0.11 arcsec and 0.39 arcsec, respectively. The corresponding integration time is 1.1 hours and 0.6

hours, respectively. The observations were performed on 11 Nov. 2016 and 03 Aug 2017, respectively. We calibrated the data individually with CASA, following the standard pipeline, then combined all visibility data together for cleaning. We selected briggs weighting with a weighting of 1.5, to optimize sensitivity and sidelobe of the dirty beam response. A final datacube with a beam size of $0.21'' \times 0.19''$ (1.47×1.27 pc) was produced. The $1-\sigma$ sensitivity is about 0.9 mJy/beam at a velocity resolution of 0.4 km/s. We listed calibrators in Table 1. The uncertainty of the absolute flux calibration is about 10% by comparing with the monitored fluxes of the ALMA calibrators.

To search for CO clumps, we first identified pixels that have a signal to noise ratio (S/N) > 3.5 in two adjacent channels of ALMA data. The search was done over the velocity range of the IRAM 30-m CO spectrum (280-290 km/s). For regions with more than ten detected pixels ($> 15\%$ beam in area), we extracted their spectra and counted those with an integrated S/N > 4 as detection. A single Gaussian profile was used to fit the spectra. In total we identified five clumps as shown in Figure 2 and listed in Table 2. To measure the size of each CO clump, we used CASA imfit() to fit a 2-D Gaussian profile to the velocity-integrated flux (moment-zero) map of the clump within a circular region. As shown in Figure 2, each circle is defined to be slightly larger than the $1-\sigma$ noise contour (2.3 mJy/beam•km/s) to include some background emission but not too large so that the enclosed pixels are dominated by noises. Note that the circle is not the size of the clump but encloses pixels over which the imfit() performed the fitting. We tested that, if the size of the circular region increases or decreases by 20%, the changes in the derived clump sizes are negligible. The imfit() also returns the associated uncertainties. The derived size dispersions (σ_{ma} , σ_{mb}) along major and minor axis were used to estimate the radius of the core: $R = D \times \tan(\sqrt{\sigma_{ma}\sigma_{mb}}) \frac{3.4}{\pi^{0.5}}$ (Solomon et al. 1987), where D is the distance of DDO 70. The defined radius represents the square root of the area of a clump. The virial mass of each core was calculated using $M_{vir} = 1040 R \sigma_v^2$ (Solomon et al. 1987), where σ_v is the line width dispersion from the spectral fitting.

2.2. Ancillary data of DDO 70

The multi-wavelength ancillary data of DDO 70 were available in the literature as compiled in our previous work (Shi et al. 2016). The infrared data at 70, 160, 250 and 350 μ m were retrieved from the archive of the *Herschel* Space Observatory and were reduced with unimap (Traficante et al. 2011). We refer readers to our previous work Shi et al. (2014, 2016) for details. The reduced

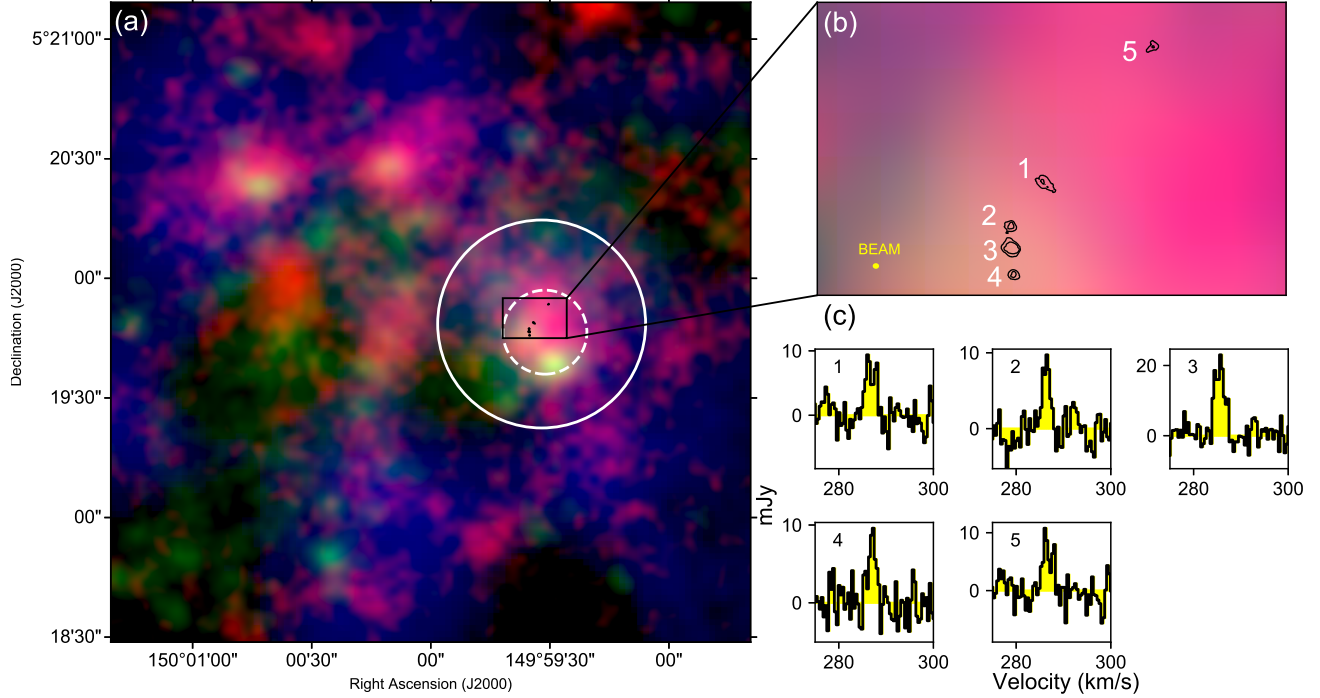


Figure 1. False color images and the ALMA interferometric data: **a**, the false color image of DDO 70 where red is for infrared emission at $160 \mu\text{m}$, green for the far-UV emission and blue for the atomic hydrogen 21 cm emission. The solid white circle indicates the ALMA FOV with the white dashed circle for the IRAM-30m FOV. Black contours are for five detected CO clumps at levels of 1.0 ($0.85\text{-}\sigma$) and $4.5 \text{ mJy}\cdot\text{km/s}/\text{beam}$ ($3.84\text{-}\sigma$). **b**, an enlarged view of detected CO clumps. **c**, the CO $J=2-1$ spectra of five detected CO clumps.

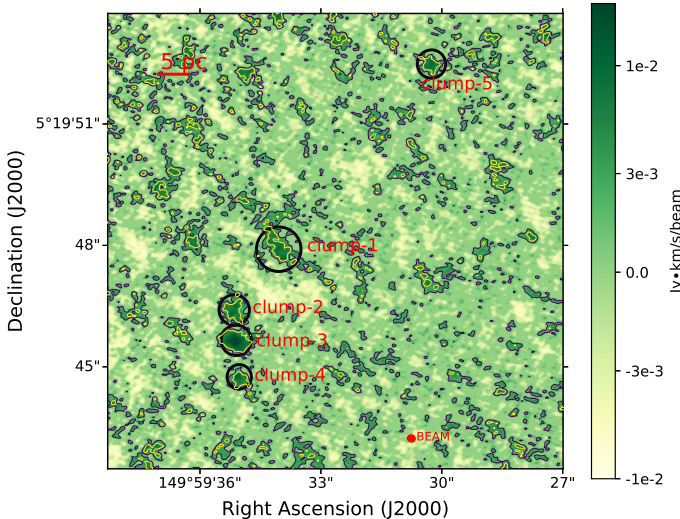


Figure 2. The ALMA CO $J=2-1$ images of five detected clumps in DDO 70. The image is the moment zero integrated from 281 to 291 km/s. Each circle denotes a region that is used for `imfit()` in CASA to obtain the size of each clump (see text). The black and yellow contours stand for $1\text{-}\sigma$ ($2.3 \text{ mJy}/\text{beam}\cdot\text{km/s}$) and $2\text{-}\sigma$ noise levels, respectively.

Spitzer images at 3.6 , 4.5 , 5.8 and $24 \mu\text{m}$ are from the

Local Volume Legacy program (Dale et al. 2009). The HI image is from the program of Local Irregulars That Trace Luminosity Extremes (Hunter et al. 2012) and the far-UV image is available in the GALEX data archive (<http://galex.stsci.edu/GalexView/>).

3. THE LARSON'S LAW

As shown in Figure 1, in total five CO clumps are detected and all of them are within the IRAM 30-m coverage in spite of the larger ALMA FOV. As listed in Table 2, the total fluxes ($127\pm 11 \text{ mJy km/s}$) of these individual clumps account for about 80% of the emission ($160\pm 30 \text{ mJy km/s}$) as seen by the IRAM 30-m telescope, indicating no significant missing fluxes. These clumps are resolved both spatially and spectroscopically with radii of $1.5\text{-}3 \text{ pc}$, velocity dispersion of $0.6\text{-}1 \text{ km/s}$ and virial masses of $0.7\text{-}3\times 10^3 M_{\odot}$. Their CO luminosities are about $20\text{-}60 \text{ K km/s pc}^2$, with the corresponding kinematic CO conversion factors of $30\text{-}120 M_{\odot} \text{ pc}^{-2} (\text{K km/s})^{-1}$.

Figure 3 shows the distributions of these CO clumps in the so-called Larson's law (Larson 1981; Solomon et al. 1987; Schruba et al. 2017) that describes the relationship between the line width and the clump radius. As shown in the figure, clumps in DDO 70 do not show systematic deviations from those in the Milky Way and the

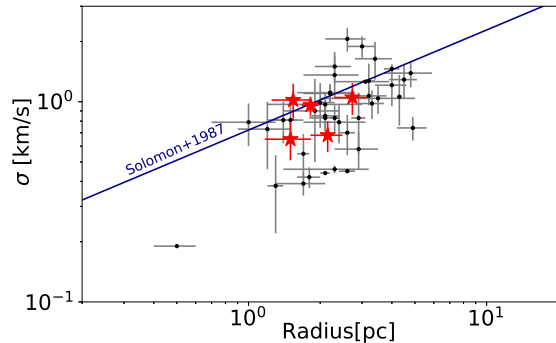


Figure 3. CO clumps in DDO 70 follow the Larson’s law of the line width vs. radius: The red star symbols denotes five clumps detected in DDO 70, with black circles for CO clumps in the dwarf NGC 6822 (Schruba et al. 2017). The green solid line is the best-fitted one of the Milky Way (Solomon et al. 1987).

dwarf galaxy NGC 6822 at 20% solar metallicity. Different interpretations have been proposed for the origin of Larson’s law: the clumps may be in virial equilibrium, which implies almost constant gas mass surface densities ($\frac{M_{\text{vir}}}{\pi r^2}$) of CO clumps from solar to 7% solar metallicity (Larson 1981; Solomon et al. 1987; Rubio et al. 2015; Schruba et al. 2017); the law could also be an observational manifestation of supersonic turbulence in which the large-scale kinetic energy injects into the ISM and cascades to small scales (Kritsuk et al. 2013), and the dynamics of clumps at pc-scales are thus still dominated by turbulence. It is difficult to differentiate these two interpretations without additional data. As discussed in Kritsuk et al. (2013), the turbulence origin could result in a flatter slope of the Larson’s law than the virial origin, but our few data points do not have enough dynamic ranges to measure the slope.

Given that the dust shielding drops with the decreasing metallicity, CO sizes should shrink. This is, however, in contrast to the fact that CO clumps in DDO 70 have similar sizes to CO clumps at higher metallicity as shown in Figure 3. We quantitatively discuss this in the following section.

4. COMPARISONS IN THE CLUMP SIZES BETWEEN DDO 70 AND THE MILKY WAY

4.1. The required shielding dust extinction for CO to exist in DDO 70

In the Milky Way, ultraviolet photons with energies larger than 11.1 eV can photo-dissociate CO molecules, so that CO emission only exists in the dust-shielded regions with a visual extinction higher than 1.0-2.0 mag (Glover et al. 2010; Bergin, & Tafalla 2007). Further studies of metal-poor dwarf galaxies including Large

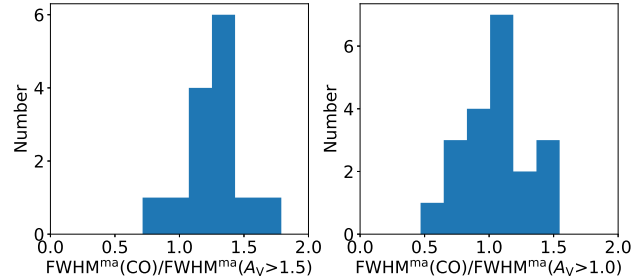


Figure 4. The ratio of CO clump sizes and dust clump sizes above two different extinction levels in the SMC.

Magellanic Cloud and Small Magellanic Cloud (SMC) confirm similar shielding conditions for CO emission. And the relationship between the CO intensity (I_{CO}) and the visual extinction (A_V) shows little dependence on the gas-phase metallicity (Leroy et al. 2009; Lee et al. 2015, 2018). Using the $I_{\text{CO}}-A_V$ relationship of the SMC (Lee et al. 2018), our CO clumps are inferred to have A_V between 1 and 2.5 mag, supporting the above required shielding for the presence of CO emission in DDO70.

To quantitatively determine the extinction levels above which dust clumps have similar sizes to CO clumps, we used the dust and CO maps of the SMC, given that the galaxy has high-S/N maps while hosting the metallicity as close as possible to our target galaxy. To produce the dust map of the SMC, the *Herschel* images were retrieved from Herschel Inventory of the Agents of Galaxy Evolution (HERITAGE) (Meixner et al. 2013) at 100, 160, 250 and 350 μm with angular resolutions of 7.7, 12, 18 and 25 arcsec, respectively. Following the previous work (Lee et al. 2015), we used the single modified black-body (MBB) model with a fixed dust emissivity of 1.5 to fit the Herschel SED to produce the dust temperature maps at 350 μm resolutions. We then interpolated this map to the 160 μm resolution and produced the extinction map using $\tau_{160\mu\text{m}} = I_{160\mu\text{m}}/B_\nu(T_{\text{dust}}, 160\mu\text{m})$ and $A_V = 2,200\tau_{160\mu\text{m}}$ (Lee et al. 2015). The CO $J=2-1$ data with an angular resolution of 28 arcsec were retrieved from the archive of the APEX telescope and reduced in a standard way. The CO clump sizes were measured in the same way as for the CO data in DDO 70. Sizes of dust clumps were measured above two A_V values of 1.0 and 1.5, respectively: we first subtracted constant A_V (1.0 or 1.5) from the extinction map of the SMC and convolved to the CO resolution, and then measured the sizes in the same way as for the CO data in DDO 70. Using spatially-resolved clumps that are defined to have sizes larger than 1.2 times the FWHM, we calculated the ratio of the major-axis FWHM of CO and the

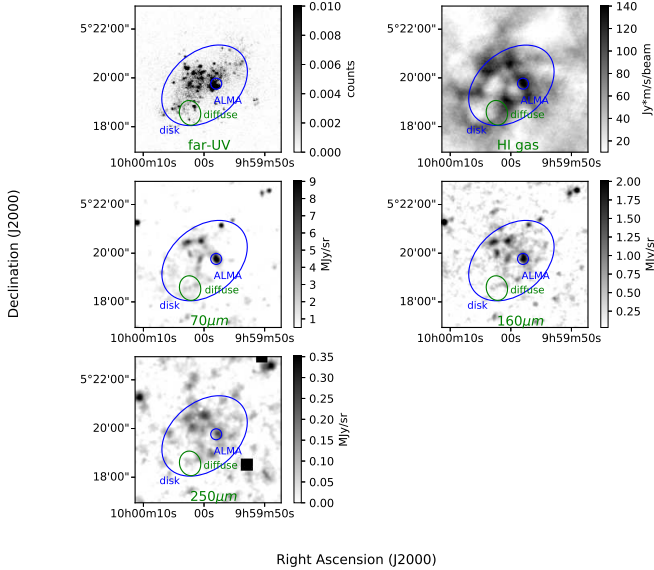


Figure 5. Multi-wavelength images of DDO70. The large blue ellipse encircles the whole disk of the galaxy. The small blue circle indicates the ALMA FOV and the green ellipse denotes the diffuse region.

FWHM of the dust emission. In total, we had 14 clumps with $A_V > 1.5$ and 20 clumps with $A_V > 1.0$, respectively. As shown in Figure 4, the median ratio with a standard deviation is 1.29 ± 0.24 for $\text{CO}/\text{dust}(A_V > 1.5)$ and 1.05 ± 0.26 for $\text{CO}/\text{dust}(A_V > 1.0)$. As a result, the dust clumps with $A_V > 1.0$ or $\tau_{160\mu\text{m}} > 1/2,200$ have similar sizes to CO clumps. Since $\tau_{160\mu\text{m}}$ is a direct measurement from the MBB fitting and thus suffers less systematic uncertainties as compared to A_V , we will adopt the limiting $\tau_{160\mu\text{m}} = 1/2,200$ in the following analysis. Although the SMC maps have poorer spatial resolutions than the maps of our DDO 70, the relationship between I_{CO} and extinction has little dependence on the spatial resolution down to sub-pc as done for the Milky Way (Lee et al. 2015, 2018), implying that the above result of the SMC likely holds at pc scales of our maps. While the $I_{\text{CO}}-A_V$ relationship shows little dependence on the metallicity from the Milky Way to the SMC at $20\%Z_{\odot}$, we here do assume that such an independence can extend to DDO 70 at $7\%Z_{\odot}$.

4.2. The gas-to-dust (GDR) ratio of DDO 70

The required extinction for CO to exist in the Milky Way ($A_V = 1.0$ mag) corresponds to a gas mass surface density of $14 M_{\odot}/\text{pc}^2$ assuming $N_{\text{H}}/A_V = 1.87 \times 10^{21} \text{ cm}^{-2} \text{ mag}^{-1}$ (Draine 2003). At lower metallicities, the required extinction corresponds to a higher gas surface density given the corresponding larger GDR, making CO suitable to trace gas of a high surface density at low

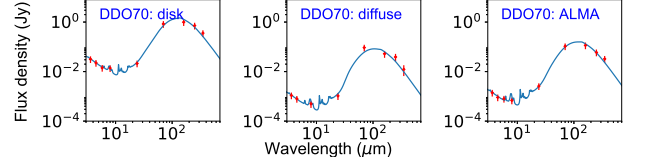


Figure 6. Infrared SEDs of the whole disk, the diffuse region and the ALMA aperture in DDO 70. Red diamonds are the *Spitzer* and *Herschel* photometry with $1-\sigma$ error bar that includes additional 30% systematic flux uncertainties. The blue line is the best-fitted dust model (Draine & Li 2007).

metallicity (Rubio et al. 2015; Schrubba et al. 2017). Arguably, one of the most reliable methods to measure the GDR at extremely low metallicity is to use the ratio of the atomic gas and the dust mass in the diffuse region where the total cold gas is dominated by the atomic gas instead of the molecular gas (Israel 1997; Dame et al. 2001; Bolatto et al. 2011; Shi et al. 2014; Jameson et al. 2016).

Following the methods of our previous work (Shi et al. 2014), we first carried out the photometric measurements of a diffuse region as well as the whole disk of DDO 70 and the region within the ALMA aperture. These regions are illustrated in Figure 5 for far-UV, HI gas, and infrared bands at 70, 160 and $250 \mu\text{m}$, respectively. The diffuse region was identified as extended emission at all *Herschel* wavelengths, not overlaid with star-formation regions, and was used to infer the gas-to-dust ratio (GDR) of the galaxy. In these regions the total cold gas is dominated by atomic gas, so the ratio of the atomic gas to the dust mass can be treated as the GDR (Leroy et al. 2011; Sandstrom et al. 2013; Shi et al. 2014). The results of *Herschel* and *Spitzer* infrared photometry were presented in Table 3. Similar to what have been done for other extremely metal-poor galaxies (Shi et al. 2014; Fisher et al. 2014), we fitted the full infrared SEDs with the DL07 dust model (Draine & Li 2007) to estimate the dust masses as shown in Figure 6 and listed in Table 4. The GDR of the galaxy is thus derived to be 6078^{+1000}_{-1600} , referred as the diffuse-region GDR. If adopting SMC or LMC dust grains, the derived ratio increases by about 10-20%. This ratio roughly corresponds to the trend of the $\text{GDR} \propto Z^{-\alpha}$ with $\alpha = 1.6$ given the Galactic GDR of 100. An α larger than unity is consistent with the fact that the dust-to-metal ratio decreases with the decreasing metallicity as measured in absorption-line systems (De Cia et al. 2013) as well as the global GDR of dwarf galaxies where the HI gas dominates the total cold gas at global galaxy scales (Rémy-Ruyer et al. 2014).

From the above measurements, we can infer other physical properties of the region within the ALMA FOV. It contains a dust mass of $530 M_{\odot}$, a total gas mass of $3.2 \times 10^6 M_{\odot}$ given the above diffuse-region GDR and a molecular gas mass of $2.7 \times 10^6 M_{\odot}$ after subtracting an HI mass of $0.53 \times 10^6 M_{\odot}$. It has a stellar mass of $1.7 \times 10^6 M_{\odot}$ and a star formation rate of $1.6 \times 10^{-4} M_{\odot}/\text{yr}$ from the $3.6 \mu\text{m}$ and $24\mu\text{m}$ +far-UV photometry, respectively, as detailed in Shi et al. (2014).

4.3. The required shielding gas surface density for CO to exist in DDO 70 and its associated uncertainty

As argued above, the size of the CO clump is set by the spatial extent above a threshold extinction ($\tau_{160\mu\text{m}}=1/2,200$) for CO to survive. This can be converted to the required gas mass surface density with $\tau_{\lambda}=\kappa_{\lambda}\Sigma_{\text{dust}}$ and the corresponding GDR of DDO 70, where κ_{λ} is the mass absorption coefficient of dust and Σ_{dust} is the dust mass surface density. We derived the required shielding gas density and its uncertainty with the following steps:

(1) The threshold $\tau_{160\mu\text{m}}$ above which the dust clump size represents the CO clump size: as discussed above, this limiting $\tau_{160\mu\text{m}}$ is $1/2,200$, and above this extinction the size of a dust clump is similar to the CO size within 26%. We thus adopted 26% as the error of the limiting $\tau_{160\mu\text{m}}$.

(2) The diffuse-region GDR of DDO 70: the diffuse-region GDR of DDO 70 is derived to be 6078^{+1000}_{-1600} , where the error reflects the photon noise plus 30% systematic flux uncertainties. Additional 15% uncertainty is included for the case if adopting different dust models (SMC or LMC) as stated above. The GDR across a galaxy is roughly constant if removing the metallicity gradient, with variation up to 50% based on spatially-resolved studies (Shi et al. 2014; Draine et al. 2014; Sandstrom et al. 2013). By adding the above three errors quadratically, we have a final uncertainty of 56%. Note that our derived GDR is near the lower bound at similar metallicities in the study of Rémy-Ruyer et al. (2014) if assuming the CO conversion factor increases with the decreasing metallicity, implying an even larger shielding gas surface density.

(3) The difference in the MBB fitting vs. DL07 dust modeling: the extinction map of the SMC used to derive the above limiting $\tau_{160\mu\text{m}}=1/2,200$ is based on the MBB fitting to the *Herschel* SED. The GDR of DDO 70 is, however, derived from the fitting to the *Spitzer*+*Herschel* SED using the DL07 dust model. This could cause some systematic offset. As a result, we added *Spitzer* photometry to the SED of the SMC and carried out DL07 dust modeling. By adopting

$\kappa_{160\mu\text{m}}=13.1 \text{ cm}^2/\text{g}$ (Weingartner & Draine 2001; Li, & Draine 2001), we obtained the DL08/MBB dust ratio of 1.89 ± 0.37 . The above GDR of DDO 70 is thus corrected to be 11487 with a $1-\sigma$ error of 59%.

(4) The drop in the GDR from the diffuse region to the dense region: the above diffuse-region GDR is derived from the diffuse region. Studies suggest a decrease in the GDR by a factor of 2-3 from the diffuse to the dense region in the Milky Way (Jenkins 2009; Planck Collaboration et al. 2011), SMC and LMC (Bot et al. 2004; Roman-Duval et al. 2014). It seems that such a decrease is not a function of the galaxy metallicity. We thus adopted a factor of 2.5 ± 0.5 to correct the above GDR to be 4,594 with a $1-\sigma$ error of 62%. We are aware of the work by Roman-Duval et al. (2017) that claims a factor of 7 drop in the GDR of the SMC from the diffuse to the dense region. However, their diffuse region has a very low gas density mainly located in the out-skirts of the SMC, resulting in a very high GDR of 1.5×10^4 that is a factor of 10 larger than other works (Bouchet et al. 1985; Gordon et al. 2009; Leroy et al. 2011; Roman-Duval et al. 2014). Such a region is different from our diffuse region which is still within the galaxy disk, and our diffuse region has $\Sigma_{\text{HI}}=11.6 M_{\odot}/\text{pc}^2$ as compared to that of the ALMA region around $21 M_{\odot}/\text{pc}^2$. We further used their result to show that the adopted drop with a factor of 2.5 ± 0.5 is approximate for our study. In DDO 70, our defined diffuse region has a dust mass surface density of $1.9 \times 10^{-3} M_{\odot}/\text{pc}^2$ that is a factor of 10 lower than that of the ALMA region. Their equations 13 and 14 give the relationships between dust mass surface densities and total cold gas mass surface densities for LMC and SMC, respectively. These two equations indicate that the GDR drops by a factor of 2.1-3.2 if the dust mass surface density increases by a factor of 10 over their observed dynamic ranges.

By adopting the above final GDR (4594 ± 2848), $\tau_{160\mu\text{m}}=1/2,200$ and $\kappa_{160\mu\text{m}}=13.1 \text{ cm}^2/\text{g}$, we derived the gas mass surface densities of CO clumps in DDO 70 to be $756 \pm 468 M_{\odot}/\text{pc}^2$.

4.4. Sizes of clumps in massive star-formation regions of the Milky Way

In order to evaluate whether gas clumps at low metallicity show some systematic differences from those at the solar metallicity, we compared clumps in DDO 70 to those in the Milky Way. We measured the clump sizes in the Milky Way using maps of gas mass surface densities of four massive star-forming regions including Cygnus X (Cao et al. 2019), NGC 6344 (Russeil et al. 2013), RCW 79 (Liu et al. 2017) and NGC 7538 (Fallscheer et al. 2013) at distances of 1.4, 1.75, 4.3 and 2.7 kpc, respec-

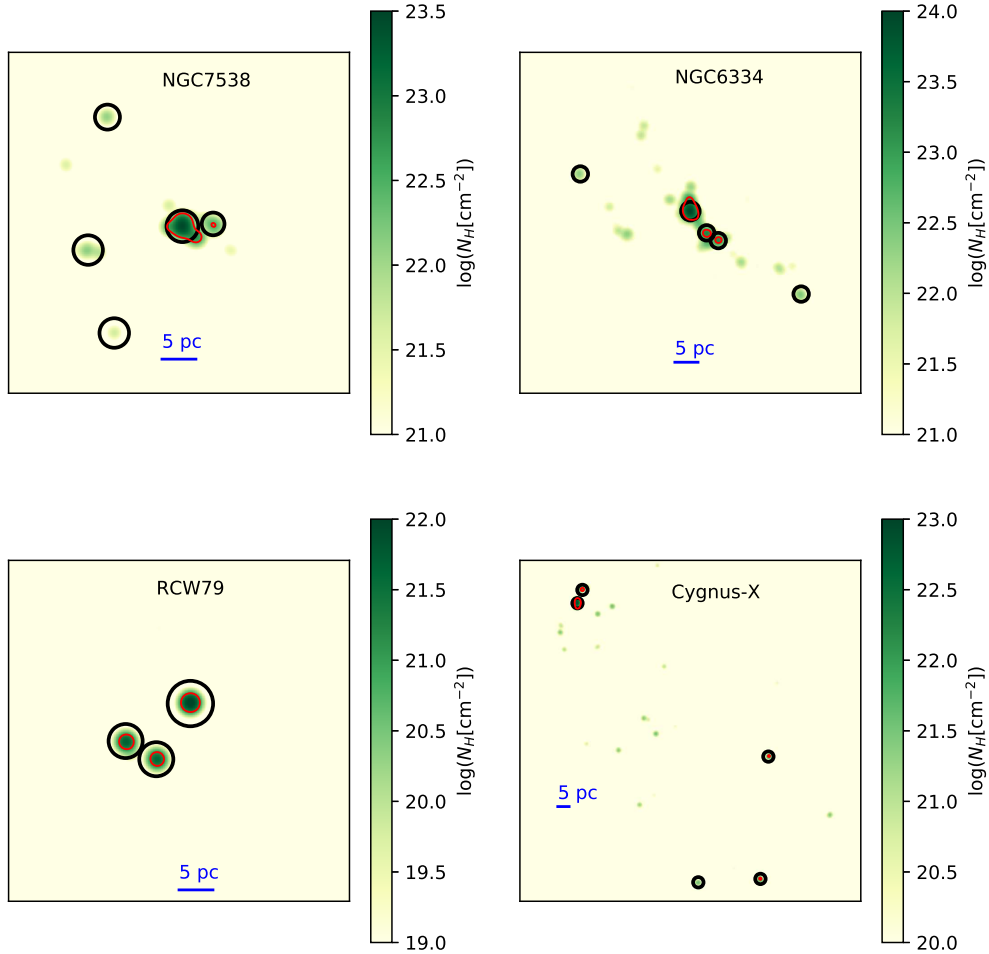


Figure 7. Maps of dust clumps with $\Sigma_{\text{gas}}^{\text{limit}} = 700 \text{ M}_{\odot} / \text{pc}^2$ in four massive star formation regions of the Milky Way. The $\Sigma_{\text{gas}}^{\text{limit}}$ is the contour level above which a clump is defined (see text). All images have the same physical pixel sizes and spatial resolutions as the CO map of DDO 70. In each panel, the red contour represents the noise level of the CO map of DDO 70 where the $1\text{-}\sigma$ noise is 10% of the peak intensity of the whole map. Clumps without red contours are small ones below the contour level. Black circles are the defined regions for $\text{imfit}()$ to fit the profiles to obtain the clump sizes. All circles are larger than the mimicked noise contour.

tively. Table 5 compares some global properties of these regions to our targeted region in DDO 70. The total cold gas mass is derived from the *Herschel* dust emission as shown below, and the SFR is estimated from the WISE $22 \mu\text{m}$ by assuming $f_{22\mu\text{m}} = f_{24\mu\text{m}}$ (Leroy et al. 2008). As listed in the table, these regions have similar global gas mass surface densities to that of DDO 70. But their global SFR surface densities are significantly larger than that in DDO 70, consistent with our previous study that the SFR efficiency is eliminated at extremely low metallicity (Shi et al. 2014).

The gas maps in the Milky Way are based on the dust maps through the MBB fitting to the *Herschel* SED with $\beta=2$, $\kappa_{300\mu\text{m}}=10 \text{ cm}^2/\text{g}$ and GDR of 100 (Beckwith et al. 1990). We further corrected these maps with two factors in order to have fair comparisons with DDO 70. The first factor is about the dust model. As shown in the

above section, the dust model for DDO 70 and SMC is the silicate-graphite-PAHs interstellar one (Weingartner & Draine 2001; Li, & Draine 2001), which gives $\kappa_{300\mu\text{m}}$ of $4.81 \text{ cm}^2/\text{g}$. As a result, we increased the original densities by a factor of 2.1. Another factor is the drop in the GDR from the diffuse region to the dense region as also discussed in the above section, which makes the gas densities decrease by a factor of 2.5. We therefore corrected the map by multiplying with a final factor of 0.83. To remove the effects of different spatial resolutions and pixel sizes on the clump size measurements, we further re-binned these maps to the same physical pixel sizes as DDO 70's CO map and convolved with Gaussian functions to the same physical spatial resolutions as DDO 70's.

Similar to what has been done for the measurements of dust clump sizes in SMC, we first subtracted a series

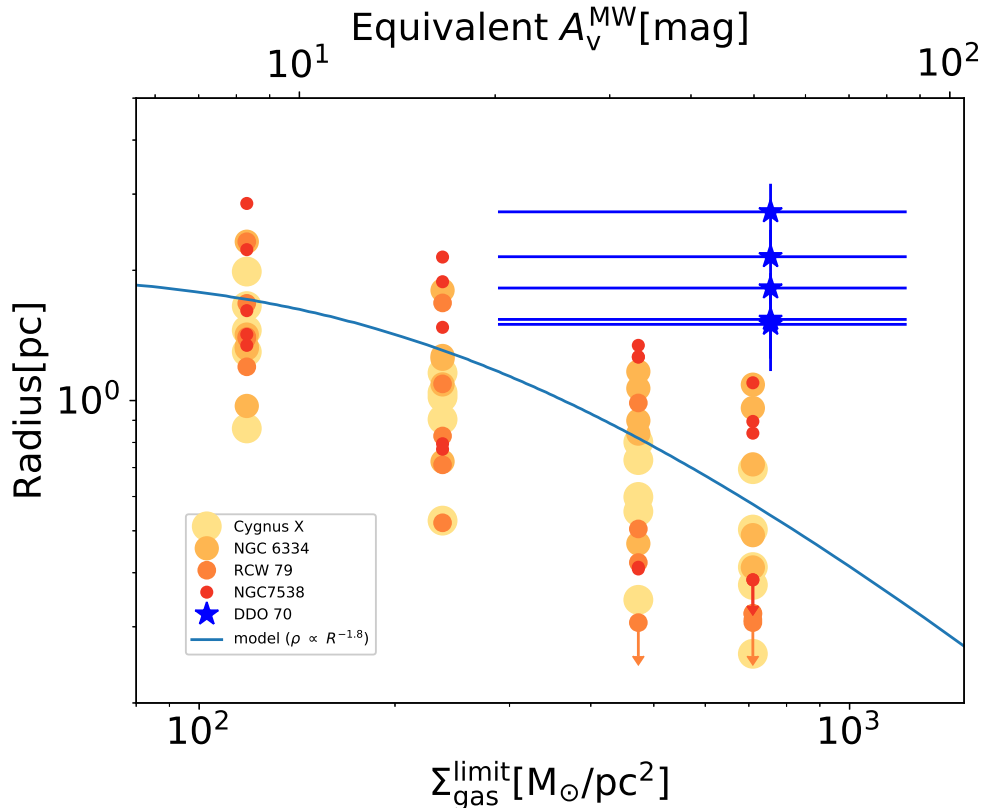


Figure 8. CO clumps in DDO 70 are significantly larger than dust clumps in massive star-formation regions of the Milky Way. The $\Sigma_{\text{gas}}^{\text{limit}}$ is the contour level above which a clump is defined. The solid line is a clump with a density profile of $R^{-1.8}$ (Mueller et al. 2002; Beuther et al. 2002). Note that, because we only detected five clumps in DDO 70, we thus compared to the five largest clumps in each massive star-formation region of the Milky Way.

of given surface densities from the whole maps of the above regions, and only used pixels with positive values. We denoted these surface densities as $\Sigma_{\text{gas}}^{\text{limit}}$, which represent the contour levels above which clumps are defined. We then used the same method as for DDO 70 to identify clumps and measured the deconvolved clump radii that were obtained by quadratically subtracting the beam size from the measured one. In the DDO 70’s CO map, the $1\text{-}\sigma$ noise is about 10% of the peak intensity of its whole map. To remove the effect of the noise in the derived clump sizes, when defining a circle for fitting a clump in the Milky Way, we make sure that the size of the circle is larger than the DDO 70’s percentage noise level that is 10% of the peak intensity of the whole map. An example is shown in Figure 7 for four Milky Way’s regions with $\Sigma_{\text{gas}}^{\text{limit}}=700 \text{ M}_{\odot}/\text{pc}^2$, and the corresponding clump sizes are listed in Table 6. As shown in the figure, some clumps are below the DDO 70’s percentage noise level, indicating that they would not have been detected in DDO 70. Such non-detection implies that the Milky Way should have on average smaller clump sizes. Since we have five detected clumps in DDO 70,

we compare them to the five largest clumps in each region of the Milky Way including those below the DDO 70’s percentage noise level. If the derived size is smaller than the *Herschel* resolution of the map, we used it as the upper-limit.

4.5. RESULTS

In Figure 8, the sizes of our CO clumps in DDO 70 were compared to those in the Milky Way at different $\Sigma_{\text{gas}}^{\text{limit}}$. Since we only detected five clumps in DDO 70, we thus only used the five largest ones in each Milky Way’s region for comparison. Note that $\Sigma_{\text{gas}}^{\text{limit}}$ is not the average gas density of a clump within its size, but the contour level above which the region is defined. In the figure, we also overlaid a modeled trend for a clump with a mass of 4000 M_{\odot} , a radius of 2.0 pc and a density profile of $\propto R^{-1.8}$. This density profile is the mean of star-forming clumps found in the Milky Way (Mueller et al. 2002; Beuther et al. 2002).

As shown in the figure, for the same $\Sigma_{\text{gas}}^{\text{limit}}$, the CO clumps in DDO70 show much larger sizes than those in the Milky Way. The mean radius of the former is

2.0 pc, while the latter has a mean of ~ 0.5 pc including upper-limits. All clumps in DDO 70 are larger than 1.5 pc while all clumps in the Milky Way at the same $\Sigma_{\text{gas}}^{\text{limit}}$ are below 1.5 pc. Even at the gas density of $288 \text{ M}_{\odot}/\text{pc}^2$ ($1\text{-}\sigma$ lower bound), DDO 70 has on average two times larger clump sizes than all four star-forming regions in the Milky Way. In the Herschel Infrared GALactic plane survey, a sample of $\sim 1.5 \times 10^4$ dense clumps has been identified and all their radii are smaller than 1.3 pc (Veneziani et al. 2017). This further excludes the statistical outliers in the Milky Way as the cause of the large clumps in DDO 70. In principle, similar analyses can be carried out for other dwarf galaxies such as WLM at $13\%Z_{\odot}$ (Elmegreen et al. 2013; Rubio et al. 2015) and NGC 6822 at $20\%Z_{\odot}$ (Schruba et al. 2017). But their relatively smaller GDR as compared to DDO 70 will make the result inconclusive due to the large error bars of the final derived gas densities as shown in the Figure 8.

The existence of large CO clumps in DDO 70 is consistent with theoretical expectation of suppressed gas fragmentation at extremely low metallicity. The high gas temperature results in a high sound speed, low Mach number and thus weak turbulence (Glover, & Clark 2012). Therefore large clumps cannot further fragment into small ones (Omukai et al. 2005). High gas temperature may also cause top-heavy stellar initial mass functions as seen both in the metal-poor LMC and high- z starburst galaxies (Zhang et al. 2018; Schneider et al. 2018). The difficulty in gas fragmentation at extremely low metallicity suggests a small number of dense clumps in which stars can form. This offers the physical origin for inefficient star formation at low metallicity (Shi et al. 2014; Filho et al. 2016; Shi et al. 2018), implying the suppression of gas fragmentation and subsequent collapse in the early Universe. Unfortunately, our result is not statistically important, given that our observation is only for one cloud. It is difficult to justify whether it is typical for all metal-poor clouds with the current data-set.

5. CONCLUSIONS

In order to probe the internal structure of a molecular cloud with an extremely low metallicity, we carried out ALMA high-spatial-resolution (1.4 pc) observations of CO emission in DDO 70, currently the most metal-poor galaxy with CO detection. Five clumps in total have been detected and account for the majority of the single-dish emission, indicating that the CO emission is mostly confined into compact regions at low metallicity. The size and velocity measurements of these clumps suggest that they follow more or less the Larson's law of

the Milky Way. A further comparison in sizes of these clumps with those in the Milky Way indicates that they have systematically larger sizes, which should not be caused by statistical outliers. The large sizes may be the result of suppressed gas fragmentation at low metallicity as large clumps cannot further fragment into small ones due to large Jeans mass and weak turbulence. As our observation is only for one region in DDO 70, it is crucial to carry out more studies to justify whether our result is representative of all types of metal-poor galaxies.

We thank the anonymous referee for his/her important and constructive suggestions that improve the quality of the paper significantly. Y.S. acknowledges the support from the National Key R&D Program of China (No. 2018YFA0404502, No. 2017YFA0402704), the National Natural Science Foundation of China (NSFC grants 11825302, 11733002 and 11773013), and the Tencent Foundation through the XPLOER PRIZE. J.W. thanks the support of NSFC (grant 11590783). YG's research is supported by National Key Basic Research and Development Program of China (grant No. 2017YFA0402704), National Natural Science Foundation of China (grant Nos. 11861131007, 11420101002), and Chinese Academy of Sciences Key Research Program of Frontier Sciences (grant No. QYZDJSSW-SLH008). This paper makes use of the following ALMA data: ADS/JAO.ALMA#2016.1.00359.S. ALMA is a partnership of ESO (representing its member states), NSF (USA) and NINS (Japan), together with NRC (Canada) and NSC and ASIAA (Taiwan) and KASI (Republic of Korea), in cooperation with the Republic of Chile. The Joint ALMA Observatory is operated by ESO, AUI/NRAO and NAOJ.

REFERENCES

- Beckwith, S. V. W., Sargent, A. I., Chini, R. S., et al. 1990, *AJ*, 99, 924
- Bergin, E. A., & Tafalla, M. 2007, *ARA&A*, 45, 339
- Beuther, H., Schilke, P., Menten, K. M., et al. 2002, *ApJ*, 566, 945
- Bolatto, A. D., Leroy, A. K., Jameson, K., et al. 2011, *ApJ*, 741, 12
- Bot, C., Boulanger, F., Lagache, G., et al. 2004, *A&A*, 423, 567
- Bouchet, P., Lequeux, J., Maurice, E., et al. 1985, *A&A*, 149, 330
- Cao, Y., Qiu, K., Zhang, Q., et al. 2019, *ApJS*, 241, 1
- Cook, D. O., Dale, D. A., Johnson, B. D., et al. 2014, *MNRAS*, 445, 899
- Dale, D. A., Cohen, S. A., Johnson, L. C., et al. 2009, *ApJ*, 703, 517
- Dame, T. M., Hartmann, D., & Thaddeus, P. 2001, *ApJ*, 547, 792
- De Cia, A., Ledoux, C., Savaglio, S., et al. 2013, *A&A*, 560, A88
- Draine, B. T. 2003, *ARA&A*, 41, 241
- Draine, B. T., & Li, A. 2007, *ApJ*, 657, 810
- Draine, B. T., Aniano, G., Krause, O., et al. 2014, *ApJ*, 780, 172
- Elmegreen, B. G., Rubio, M., Hunter, D. A., et al. 2013, *Nature*, 495, 487
- Fallscheer, C., Reid, M. A., Di Francesco, J., et al. 2013, *ApJ*, 773, 102
- Filho, M. E., Sánchez Almeida, J., Amorín, R., et al. 2016, *ApJ*, 820, 109
- Fisher, D. B., Bolatto, A. D., Herrera-Camus, R., et al. 2014, *Nature*, 505, 186
- Glover, S. C. O., Federrath, C., Mac Low, M.-M., et al. 2010, *MNRAS*, 404, 2
- Glover, S. C. O., & Clark, P. C. 2012, *MNRAS*, 426, 377
- Gordon, K. D., Bot, C., Muller, E., et al. 2009, *ApJL*, 690, L76
- Hunt, L. K., Testi, L., Casasola, V., et al. 2014, *A&A*, 561, A49
- Hunter, D. A., Ficut-Vicas, D., Ashley, T., et al. 2012, *AJ*, 144, 134
- Inoue, A. K., Tamura, Y., Matsuo, H., et al. 2016, *Science*, 352, 1559
- Israel, F. P. 1997, *A&A*, 328, 471
- Jameson, K. E., Bolatto, A. D., Leroy, A. K., et al. 2016, *ApJ*, 825, 12
- Jenkins, E. B. 2009, *ApJ*, 700, 1299
- Kritsuk, A. G., Lee, C. T., & Norman, M. L. 2013, *MNRAS*, 436, 3247
- Knudsen, K. K., Richard, J., Kneib, J.-P., et al. 2016, *MNRAS*, 462, L6
- Kniazev, A. Y., Grebel, E. K., Pustilnik, S. A., et al. 2005, *AJ*, 130, 1558
- Larson, R. B. 1981, *MNRAS*, 194, 809
- Lee, C., Leroy, A. K., Schnee, S., et al. 2015, *MNRAS*, 450, 2708
- Lee, C., Leroy, A. K., Bolatto, A. D., et al. 2018, *MNRAS*, 474, 4672
- Leroy, A. K., Walter, F., Brinks, E., et al. 2008, *AJ*, 136, 2782
- Leroy, A. K., Bolatto, A., Bot, C., et al. 2009, *ApJ*, 702, 352
- Leroy, A. K., Bolatto, A., Gordon, K., et al. 2011, *ApJ*, 737, 12
- Li, A., & Draine, B. T. 2001, *ApJ*, 554, 778
- Liu, H.-L., Figueira, M., Zavagno, A., et al. 2017, *A&A*, 602, A95
- Madau, P., & Dickinson, M. 2014, *ARA&A*, 52, 415
- Meixner, M., Panuzzo, P., Roman-Duval, J., et al. 2013, *AJ*, 146, 62
- Mueller, K. E., Shirley, Y. L., Evans, N. J., et al. 2002, *ApJS*, 143, 469
- Omukai, K., Tsuribe, T., Schneider, R., et al. 2005, *ApJ*, 626, 627
- Planck Collaboration, Abergel, A., Ade, P. A. R., et al. 2011, *A&A*, 536, A24
- Rémy-Ruyer, A., Madden, S. C., Galliano, F., et al. 2014, *A&A*, 563, A31
- Roman-Duval, J., Gordon, K. D., Meixner, M., et al. 2014, *ApJ*, 797, 86
- Roman-Duval, J., Bot, C., Chastenet, J., et al. 2017, *ApJ*, 841, 72
- Rubio, M., Elmegreen, B. G., Hunter, D. A., et al. 2015, *Nature*, 525, 218
- Russeil, D., Schneider, N., Anderson, L. D., et al. 2013, *A&A*, 554, A42
- Sandstrom, K. M., Leroy, A. K., Walter, F., et al. 2013, *ApJ*, 777, 5
- Schneider, F. R. N., Sana, H., Evans, C. J., et al. 2018, *Science*, 359, 69
- Schruba, A., Leroy, A. K., Kruijssen, J. M. D., et al. 2017, *ApJ*, 835, 278
- Shi, Y., Armus, L., Helou, G., et al. 2014, *Nature*, 514, 335
- Shi, Y., Wang, J., Zhang, Z.-Y., et al. 2015, *ApJ*, 804, L11
- Shi, Y., Wang, J., Zhang, Z.-Y., et al. 2016, *Nature Communications*, 7, 13789
- Shi, Y., Yan, L., Armus, L., et al. 2018, *ApJ*, 853, 149
- Sobral, D., Best, P. N., Smail, I., et al. 2014, *MNRAS*, 437, 3516

- Solomon, P. M., Rivolo, A. R., Barrett, J., et al. 1987, *ApJ*, 319, 730
- Traficante, A., Calzoletti, L., Veneziani, M., et al. 2011, *MNRAS*, 416, 2932
- Tully, R. B., Courtois, H. M., Dolphin, A. E., et al. 2013, *AJ*, 146, 86
- Veneziani, M., Schisano, E., Elia, D., et al. 2017, *A&A*, 599, A7
- Weingartner, J. C., & Draine, B. T. 2001, *ApJ*, 548, 296
- Zhang, Q., Wang, Y., Pillai, T., et al. 2009, *ApJ*, 696, 268
- Zhang, Z.-Y., Romano, D., Ivison, R. J., et al. 2018, *Nature*, 558, 260

Table 1. ALMA observational information.

SB name	DDO70_a.06.TM2	DDO70_a.06.TM1
Array configuration	C40-4	C40-7
Observing Date	11-Nov-2016	03-Aug-2017
Bandpass Calibrator	J1058+0133	J1058+0133
Flux Calibrator	J0854+2006	J1037-2934
Gain Calibrator	J1008+0621	J1008+0621
Integration Time (s)	2177	3810
Median PWV (mm)	0.55	0.7
Angular Resolution (")	0.35	0.10

NOTE—PWV stands for precipitable water vapour

Table 2. Properties of CO $J=2-1$ clumps in DDO 70.

region	RA(J2000)	DEC(J2000)	FWHM _{ma} (pc)	FWHM _{mb} (pc)	Radius (pc)	σ_v (km/s)	$S_{\text{CO}}\Delta V$ (mJy km/s)	M_{vir} (M_{\odot})	L_{CO} (K km/s pc ²)
clump-1	9:59:58.270	+5:19:47.88	5.23±1.07	2.14±0.54	2.73±0.44	1.05±0.19	22.3±5.2	3102.1±1239.4	25.9±6.0
clump-2	9:59:58.344	+5:19:46.37	2.75±0.60	2.55±0.54	2.15±0.33	0.68±0.12	16.4±3.3	1050.1±398.1	19.1±3.8
clump-3	9:59:58.343	+5:19:45.62	2.88±0.33	1.74±0.20	1.82±0.15	0.96±0.10	51.1±6.8	1751.7±398.3	59.4±7.9
clump-4	9:59:58.336	+5:19:44.72	1.88±0.54	1.81±0.60	1.50±0.33	0.65±0.14	16.1±4.0	662.0±319.8	18.7±4.7
clump-5	9:59:58.019	+5:19:52.42	2.55±0.60	1.41±0.40	1.54±0.29	1.02±0.21	21.8±5.4	1679.9±763.4	25.4±6.3

Table 3. Infrared photometry of the whole disk, diffuse region and ALMA aperture of DDO 70.

region	Right ascension (J2000)	Declination (J2000)	sizes(ma,mb) (arcsec)	f(3.6 μm) (mJy)	f(4.5 μm) (mJy)	f(5.8 μm) (mJy)	f(8.0 μm) (mJy)	f(24 μm) (mJy)	f(70 μm) (mJy)	f(160 μm) (mJy)	f(250 μm) (mJy)	f(350 μm) (mJy)
disk	09 59 59.9	+05 19 42	118.5x82.7	31.74±0.03	22.51±0.04	14.19±0.16	13.82±0.15	21.37±0.47	839±16	992±17	720± 23	357± 17
diffuse	10 00 02.3	+05 18 34	30.6x26.0	1.09±0.01	0.79±0.01	<0.19	0.50±0.06	1.04±0.11	92±3	52±4	38±5	13±4
ALMA	09 59 58.0	+05 19 46	13.5x13.5	1.41±0.01	0.91±0.01	0.80±0.03	0.69±0.03	2.58±0.05	105±1	114±2	59±3	32±3

Table 4. The fitting results of the infrared SEDs.

region	U_{min}	$U_{\text{max}}(\text{fixed})$	γ	χ^2/dof	M_{dust} (M_{\odot})	$M_{\text{HI}}/M_{\text{dust}}$
DDO70/disk	3.0	10 ⁶	0.00	1.95	(7.2 ^{+2.4} _{-1.5})x10 ³	(2.2 ^{+0.4} _{-0.7})x10 ³
DDO70/diff-1	7.0	10 ⁶	0.00	3.06	(2.1 ^{+0.6} _{-0.4})x10 ²	(6.1 ^{+0.4} _{-0.7})x10 ³
DDO70/ALMA	5.0	10 ⁶	0.00	1.08	(5.3 ^{+1.3} _{-1.0})x10 ²	(1. ^{+0.4} _{-0.7})x10 ³

NOTE—In addition to the flux uncertainties in Table 3, absolute calibration errors (20%) are included when performing the fits.

Table 5. Global properties of star-formation regions in DDO 70 and the Milky Way.

region	D	area	M_{gas}	Σ_{gas}	SFR	Σ_{SFR}
	(kpc)	(pc ²)	(M _⊙)	(M _⊙ /pc ²)	(M _⊙ /yr)	(M _⊙ /yr/kpc ²)
DDO 70 (ALMA FOV)	1.38×10 ³	2.46×10 ⁴	3.2×10 ⁶	130	1.6×10 ⁻⁴	6.4×10 ⁻³
NGC 6334 (Herschel FOV)	1.75	2.30×10 ³	4.1×10 ⁵	179	5.0×10 ⁻⁴	0.22
Cygnus-X (Herschel FOV)	1.40	1.44×10 ⁴	1.6×10 ⁶	109	1.4×10 ⁻³	0.10
RCW 79 (Herschel FOV)	4.30	1.50×10 ³	1.8×10 ⁵	122	2.1×10 ⁻⁴	0.14
NGC 7538 (Herschel FOV)	2.70	2.14×10 ³	3.3×10 ⁵	156	1.1×10 ⁻⁴	0.05

NOTE—All associated errors are dominated by the systematic uncertainties. The gas mass of DDO 70 has an error around 30%, while those in the Milky Way is around 10%. All SFRs have errors around 20%.

Table 6. Sizes of dust clumps with $\Sigma_{\text{gas}}^{\text{limit}}=700 \text{ M}_{\odot}/\text{pc}^2$ in massive star-formation regions of the Milky Way.

Region	FWHM _{ma}	FWHM _{mb}	Radius
	(pc)	(pc)	(pc)
Cygnus-X	2.04±0.08	0.36±0.15	0.69±0.14
Cygnus-X	0.58±0.10	0.36±0.16	0.37±0.09
Cygnus-X	0.41±0.00	0.25±0.00	0.26±0.00
Cygnus-X	0.95±0.03	0.27±0.09	0.41±0.07
Cygnus-X	1.03±0.10	0.37±0.25	0.50±0.18
NGC6334	1.84±0.09	0.96±0.07	1.09±0.05
NGC6334	1.43±0.27	0.97±0.29	0.96±0.17
NGC6334	1.16±0.31	0.66±0.32	0.71±0.20
NGC6334	0.92±0.03	0.27±0.09	0.41±0.07
NGC6334	0.89±0.03	0.40±0.04	0.49±0.03
RCW79	0.40±0.00	0.37±0.00	0.31±0.00
RCW79	0.50±0.03	0.31±0.04	0.32±0.02
RCW79	0.50±0.00	0.31±0.01	0.32±0.00
NGC7538	1.58±0.12	1.23±0.10	1.13±0.06
NGC7538	1.41±0.22	0.75±0.26	0.84±0.16
NGC7538	0.43±0.00	0.39±0.00	0.33±0.00
NGC7538	2.39±0.25	0.50±0.38	0.89±0.34
NGC7538	0.40±0.00	0.32±0.00	0.29±0.00